

Article

Operando NAP-XPS Studies of a Ceria-Supported Pd Catalyst for CO Oxidation

 Xènia Garcia ^{1,2} , Lluís Soler ¹ , Xavier Vendrell ¹ , Isabel Serrano ¹ , Facundo Herrera ^{2,3} , Jordi Prat ², Eduardo Solano ² , Massimo Tallarida ², Jordi Llorca ^{1,*}  and Carlos Escudero ^{2,*} 

¹ Institute of Energy Technologies, Department of Chemical Engineering and Barcelona Research Center in Multiscale Science and Engineering, Universitat Politècnica de Catalunya, EEBE, Eduard Maristany 10-14, 08019 Barcelona, Spain

² ALBA Synchrotron Light Source, Carrer de la Llum 2-26, 08290 Cerdanyola del Vallès, Spain

³ Instituto de Investigaciones Fisicoquímicas Teóricas y Aplicadas (INIFTA, CONICET), Departamento de Química, Facultad de Ciencias Exactas, Universidad Nacional de La Plata, Diagonal 113 y 64, La Plata 1900, Argentina

* Correspondence: jordi.llerca@upc.edu (J.L.); cescudero@cells.es (C.E.)

Abstract: Supported Pd/CeO₂ catalytic systems have been widely investigated in the low-temperature oxidation of CO (LTO CO) due to the unique oxygen storage capacity and redox properties of the ceria support, which highly influence the structural, chemical and electronic state of Pd species. Herein, *operando* near-ambient pressure XPS (NAP-XPS) technique has allowed the study of a conventional Pd/CeO₂ catalyst surface during the CO oxidation reaction under experimental conditions closer to the actual catalytic reaction, unfeasible with other surface science techniques that demand UHV conditions. SEM, HRTEM and XRD analyses of the powder catalyst, prepared by conventional incipient wetness impregnation, reveal uniformly CeO₂-loaded Pd NPs of less than 2 nm size, which generated an increase in oxygen vacancies with concomitant ceria reduction, as indicated by H₂-TPR and Raman measurements. Adsorbed peroxide (O₂²⁻) species on the catalyst surface could also be detected by Raman spectra. *Operando* NAP-XPS results obtained at the ALBA Synchrotron Light Source revealed two kinds of Pd species under reaction conditions, namely PdO_x and Pd^{II} ions in a Pd_xCe_{1-x}O_{2-δ} solution, the latter one appearing to be crucial for the CO oxidation. By means of a non-destructive depth profile analysis using variable synchrotron excitation energies, the location and the role of these palladium species in the CO oxidation reaction could be clarified: PdO_x was found to prevail on the upper surface layers of the metallic Pd supported NPs under CO, while under reaction mixture it was rapidly depleted from the surface, leaving a greater amount in the subsurface layers (7% vs. 12%, respectively). On the contrary, the Pd_xCe_{1-x}O_{2-δ} phase, which was created at the Pd–CeO₂ interface in contact with the gas environment, appeared to be predominant on the surface of the catalyst. Its presence was crucial for CO oxidation evolution, acting as a route through which active oxygen species could be transferred from ceria to Pd species for CO oxidation.

Keywords: palladium catalyst; cerium oxide; CO oxidation; NAP-XPS; metal–support interaction



Citation: Garcia, X.; Soler, L.; Vendrell, X.; Serrano, I.; Herrera, F.; Prat, J.; Solano, E.; Tallarida, M.; Llorca, J.; Escudero, C. *Operando* NAP-XPS Studies of a Ceria-Supported Pd Catalyst for CO Oxidation. *Chemistry* **2023**, *5*, 1–18. <https://doi.org/10.3390/chemistry5010001>

Academic Editors: José Antonio Odriozola and Hermenegildo García

Received: 22 November 2022

Revised: 15 December 2022

Accepted: 16 December 2022

Published: 20 December 2022



Copyright: © 2022 by the authors. Licensee MDPI, Basel, Switzerland. This article is an open access article distributed under the terms and conditions of the Creative Commons Attribution (CC BY) license (<https://creativecommons.org/licenses/by/4.0/>).

1. Introduction

Ceria or cerium dioxide exhibits very interesting redox properties given its electronic configuration ([Xe] 6s²5d¹4f¹). The ability to easily change between Ce^{III} and Ce^{IV} oxidation states and the capacity to accommodate oxygen vacancies on its structure (Equation (1)), known as oxygen storage capacity (OSC) [1], makes ceria a ubiquitous constituent in catalytic systems for different applications. For instance, the oxide can be used as a catalytic support for many chemical reactions, such as alcohol oxidation [2], soot combustion [3] or carbon monoxide oxidation [4]:



Nevertheless, the most known application of CeO₂-based materials is as a component in automotive three-way catalysts (TWCs) [5,6]. Mounted after an internal combustion engine, the TWC's role is to remove the pollutants produced by fuel combustion, promoting simultaneously the oxidation of CO and unburnt hydrocarbons, as well as the reduction of nitrogen oxides (NO_x). The catalytic material of the early TWCs consisted of a thermally stable support (doped Al₂O₃), and active metallic phase (Pt, Pd, Rh) and a CeO₂ promoter [7]. Nowadays, the so-called advanced TWCs employ CexZr1-xO2 solid solutions instead of pure ceria [8]. Besides this well-established use, ceria is emerging as a unique material, holding great promise for future market breakthroughs, such as a component of solid oxide fuel cells (SOFCs), a solid state electrolyte oxygen type sensor and as an antioxidant agent for biomedical applications [9]. As CO oxidation is a primary function of TWCs containing ceria, it has often been used as a probe reaction over ceria-based materials to evaluate different catalyst formulations and their redox properties. It is accepted that CO oxidation proceeds through the Mars–Van Krevelen mechanism over ceria, that is, lattice oxygen atoms of the ceria surface are transferred to CO, and the vacancies created on the oxide are subsequently filled by gaseous oxygen [10]. The formation of oxygen vacancies is the rate determining step, since the replenishment with gas-phase O₂ is favorable for reduced ceria [11].

Catalyst design usually includes a support with adequate redox properties loaded with a metallic active phase. Palladium is one of the most active metals interacting with the surface of oxides, and it is characterized by a relatively high affinity with oxygen. In fact, the Pd/CeO₂ catalytic system has been extensively studied and employed as a component in multiple catalytic reactions, such as the low-temperature oxidation of CO (LTO CO) [12], the water–gas shift (WGS) reaction [13,14], and CH_x oxidation [15], but the main application of this system is as a component of the aforementioned TWCs' exhaust gas purification systems. It is well known that the catalytic activity of Pd nanoparticles, as occurs with other metals, is closely related *inter alia* to their size, shape and valence state [16]. Thus, it is of great importance to stabilize Pd nanoparticles under various reaction conditions, preventing variations on the particle size, shape or physicochemical states that could ultimately affect their catalytic properties. Cerium oxide is widely used as a support to load palladium nanoparticles [13,14], considering its oxygen storage capacity and its redox properties, in order to influence the chemical and electronic states of Pd species [5] and stabilize Pd nanoparticles against sintering [17]. For supported Pd catalysts, the influence of the support nature on their catalytic performance is usually described by the interaction between the support and the Pd or PdO species [18]. Many studies proposed the formation of solid solutions of Pd_xCe_{1-x}O₂ at the surface and subsurface layers of the ceria lattice [12,19], and quantum-chemical calculations have confirmed the formation of these structures in the Pd/CeO₂ systems [20,21]. In another work, Colussi et al. reported the formation of Pd–O–Ce superstructures on the ceria (110) surface [22]. However, some researchers consider that the oxidation state of Pd highly active in LTO CO is related to PdO or PdO₂ nanoparticles confined inside the support oxide matrix [19,23]. Despite extensive investigations, the exact electronic and geometric structure of the Pd/CeO₂ active centers and the role of the ceria support are still ambiguous.

Additionally, although a large number of catalytic studies in surface chemistry have been performed using different surface science techniques requiring ultrahigh vacuum (UHV) conditions [24], it has been found that under experimental conditions closer to the ones used for the actual catalytic reactions, the reaction mechanisms and catalyst architectures can differ from those under UHV conditions [25]. Indeed, some structures and catalytic active sites may only develop under specific reaction conditions, making the application of *in situ* or *operando* techniques indispensable to identify and understand the behavior of these working active species. In the last years, such *operando* techniques have been increasingly applied. Among them, near ambient pressure X-ray photoelectron spectroscopy (NAP-XPS) has become a key tool to study active sites under more realistic conditions, owing to its sensitivity to the surface and sub-surface of catalysts [26].

In the present study, CO oxidation reaction is investigated by NAP-XPS on a polycrystalline Pd/CeO₂ powder catalyst prepared by conventional incipient wetness impregnation. Since contradictory data concerning the nature of Pd–Ce–O species active in the CO oxidation reaction still persist, this work aims to provide a comprehensive investigation of the interaction between Pd and the support surface and determine its structural and electronic state during LTO CO by using NAP-XPS, as well as other characterization techniques.

2. Materials and Methods

2.1. Catalyst Preparation

Pd/CeO₂ catalyst was prepared by incipient wetness impregnation [27] from a palladium nitrate solution (Alfa Aesar, 99.9%) over CeO₂ polycrystals, synthesized following reported methods [28]. Briefly, 35 mL of an aqueous solution of 6.07 g of Ce(NO₃)₃ (99.5%, Alfa Aesar, Ward Hill, MA, US) was electrosprayed over 245 mL of an aqueous solution containing 1.96 g of NaOH (97%, Fisher Scientific, Waltham, MA, US) under vigorous stirring, using an ultrasonic atomizer (Sonozap HTWS30, Melville, NY, US). The resultant suspension was agitated for 30 min at room temperature and was then transferred into a PTFE-lined stainless-steel autoclave (Reactor Chemipress-500, Trallero And Schlee, La Llagosta, Spain), where it was heated to 150 °C for 24 h. After the hydrothermal treatment, the resulting mixture was cooled and separated by centrifugation (10 min at 6000 rpm), washed three times with deionized water and three times with ethanol. The powder was finally dried at 60 °C in air overnight [29]. As already mentioned, once the support was prepared, a palladium nitrate solution was deposited dropwise by incipient wetness impregnation in order to obtain a Pd loading of 4 wt%. After impregnation, the powder was dried overnight at 100 °C and then calcined in air at 500 °C for 5 h (1 °C·min⁻¹) to generate the Pd nanoparticles.

2.2. Catalyst Characterization

Surface morphology was evaluated using scanning electron microscopy (SEM). The images were acquired with a Zeiss Neon40 Crossbeam Station instrument at 5 kV equipped with a field emission source. The sample was prepared by placing a drop of a suspension of the Pd/CeO₂ powder catalyst in methanol on a silicon wafer and allowed to dry. High resolution transmission electron microscopy (HRTEM) images were obtained by using a field emission gun FEI Tecnai F20 microscope equipped with a field emission source at an accelerating voltage of 200 kV, with a point-to-point resolution of 0.19 nm. The sample was prepared by depositing a drop from a methanol suspension of the catalyst on a holey carbon-coated copper grid and allowing them to evaporate. The average particle diameter was calculated from the mean diameter frequency distribution with the formula: $d = \sum n_i d_i / \sum n_i$, where n_i is the number of particles with particle diameter d_i in a certain range.

Powder X-ray Diffraction (XRD) patterns were recorded with a Siemens D5000 diffractometer using Cu K α radiation (45 kV, 35 mA) in Bragg–Brentano geometry. The diffraction patterns were recorded in steps of 0.02° and 1 s per step using a 2 θ range from 10 to 80°. Crystallite sizes were estimated from the XRD data using the Debye–Scherrer equation.

Micro-Raman spectroscopy was performed using a commercial Renishaw inVia Qontor confocal Raman microscope. The Raman setup consists of a laser (at 532 nm with a nominal 100 mW output power) directed through a microscope (a specially adapted Leica DM2700 M microscope) to the sample, after which the scattered light is collected and directed to a spectrometer with a 2400 lines·mm⁻¹ grating. The laser power was adjusted to 1% of its nominal output power, the exposure time was 0.5 s, and spectra were collected with 50 accumulations.

Temperature programmed reduction with hydrogen (H₂-TPR) was carried out in a quartz U-tube with a Chemstar TPX chemisorption analyzer (Quantachrome Instruments, Boynton Beach, FL, USA) equipped with a Thermal Conductivity Detector (TCD). Initially, 30 mg of sample were pre-treated, heating them from room temperature to 450 °C in argon

flow ($50 \text{ mL}\cdot\text{min}^{-1}$, $10 \text{ }^\circ\text{C}\cdot\text{min}^{-1}$), over 30 min. The samples were then cooled down to $50 \text{ }^\circ\text{C}$ under the same atmosphere, and the H_2 -TPR experiments were conducted by heating from $50 \text{ }^\circ\text{C}$ up to $850 \text{ }^\circ\text{C}$ ($10 \text{ }^\circ\text{C}\cdot\text{min}^{-1}$) under 10% H_2 in Ar (with a total flow of $50 \text{ mL}\cdot\text{min}^{-1}$), while monitoring the hydrogen consumption with a TCD detector. The temperature was kept for 30 min at $850 \text{ }^\circ\text{C}$.

NAP-XPS was conducted at the NAPP end station of the CIRCE beamline at the ALBA Synchrotron Light Source, following the surface chemical composition under *operando* conditions at different temperatures, gas environments (H_2 , CO and CO + O_2) and pressures. Different excitation photon energies were used to obtain XP spectra of Ce 3d, O 1s, Pd 3d, C 1s and Si 2p from two different sample depths (acquiring photoelectrons with 150 and 450 eV kinetic energies, corresponding approximately to 0.5 and 1.0 nm inelastic mean free paths, respectively). Pd/CeO₂ catalyst powder was pressed with a gold mesh with 0.25 mm of nominal aperture (99.9%, GoodFellow) to form a compact disk and minimize charging effects. NAP-XPS measurements were acquired with a commercial PHOIBOS 150 NAP energy analyzer, equipped with four differentially pumped stages [25]. Hydrogen gas for the preliminary reduction of the catalysts was dosed into the analysis chamber by a leak valve, while the carbon monoxide and the carbon monoxide/oxygen reaction mixture (CO:O₂ = 2:1, $15 \text{ mL}\cdot\text{min}^{-1}$ total flow) were introduced by using mass flow controllers and active pumping to control the final pressure (1.5 mbar). The evolution of products was followed by a quadrupole mass spectrometer Microvision Residual Gas Analyzer (MKS Instruments). The sequence of spectra recorded and experiments performed was: (i) sample pre-treatment by reduction under 1 mbar of H_2 from room temperature to $350 \text{ }^\circ\text{C}$, (ii) cooling down to $250 \text{ }^\circ\text{C}$, H_2 removal and introduction of $10 \text{ mL}\cdot\text{min}^{-1}$ of CO at $250 \text{ }^\circ\text{C}$ and 1 mbar, (iii) CO oxidation at $250 \text{ }^\circ\text{C}$ by adding $5 \text{ mL}\cdot\text{min}^{-1}$ of O_2 to the previous flow of CO at $250 \text{ }^\circ\text{C}$ (CO oxidation, CO:O₂ = 2:1, total pressure of 1.5 mbar), (iv) CO oxidation at $300 \text{ }^\circ\text{C}$, and (v) CO oxidation at $350 \text{ }^\circ\text{C}$. The sample was heated using an infrared laser ($\lambda = 808 \text{ nm}$) focused on a stainless-steel plate, on top of which it was mounted. The temperature was monitored with a K-type thermocouple in contact with the samples. Data processing was performed with the CasaXPS program (Casa Software Ltd., Teignmouth, UK). To compensate charging effects, spectra were calibrated considering the C 1s peak at 284.8 eV and the U''' Ce 3d peak at 916.9 eV. A Shirley-type background was subtracted from each spectrum, and all spectra were fitted using a product of Lorentzian and Gaussian functions, except for the metallic components in the Pd 3d region, which were fitted through an asymmetric line shape. Atomic fractions were calculated using peak areas normalized on the basis of acquisition parameters after background subtraction. Cerium 3d spectra were deconvoluted using six peaks for Ce^{IV} (V, V'', V''', U, U'' and U'''), which correspond to three pairs of spin-orbit doublets, and four peaks for Ce^{III} (V₀, V', U₀ and U'), corresponding to two doublets, based on the peak positions reported by Mullins et al. [30], where U and V refer to the $3d_{3/2}$ and $3d_{5/2}$ spin-orbit components, respectively.

3. Results and Discussion

3.1. Characterization

The morphology of the CeO₂ powder was analyzed by SEM before the deposition of Pd for the preparation of the Pd/CeO₂ sample. The obtained images showed that ceria polycrystals have an irregular rounded morphology and range from about 5 to 20 nm in size, as illustrated in Figure 1. Palladium deposition modified neither the morphology nor the size distribution of ceria polycrystals. Metallic nanoparticles could not be identified with the backscattered electron signal due to their small size (see Figure 1b).

HRTEM measurements of the Pd/CeO₂ catalyst proved the presence of isolated palladium nanoparticles of less than 2 nm in diameter very well dispersed over ceria polycrystals, as seen in Figure 1c,d. Ceria polycrystals presented a mean size of $7 \pm 3 \text{ nm}$, in accordance with SEM results. The Fourier transform images showed spots corresponding to the (111), (200) and (220) planes of the ceria fcc structure at 3.1, 2.7 and 1.9 Å, respectively. As expected, the XRD pattern of CeO₂ polycrystals (Figure 2) showed the characteristic

reflections of the CeO_2 fcc phase [23,31]. After Pd deposition, a small peak corresponding to Pd (111) could be discerned, while no sign of PdO phase, easily generated in the calcination process under air, could be identified. Ceria nanoparticles presented an average crystallite size of 14 nm, as estimated from the Debye–Scherrer formula. These results are in good accordance with SEM and HRTEM images.

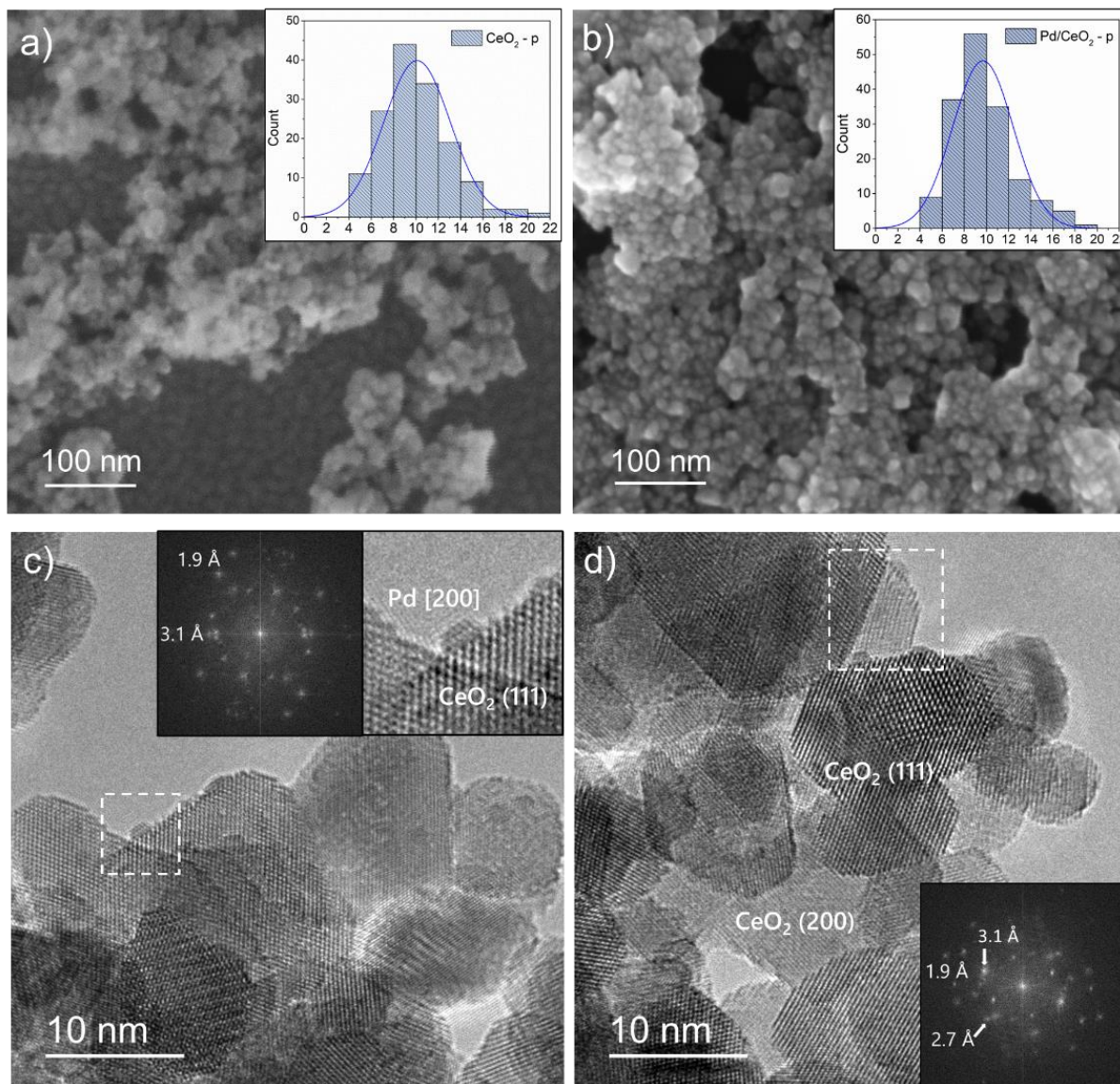


Figure 1. SEM images of ceria polycrystals (a) before and (b) after Pd deposition (Pd/CeO_2), and (c,d) HRTEM images of the Pd/CeO_2 catalyst with their corresponding Fourier transform (FT) images.

Figure 3 shows the Raman spectra of the as-synthesized samples collected at room temperature. Generally, four peaks are observed in the Raman spectra of bare CeO_2 : the main peak at 462 cm^{-1} (F_{2g}) is ascribed to the symmetric stretch mode of oxygen ions in the $[\text{CeO}_8]$ cubic subunit characteristic of the ceria fluorite lattice structure, and three weak peaks discerned at approximately 255 , 595 and 1180 cm^{-1} . These bands are due to the second-order transverse acoustic (2TA) mode, the defect-induced (D) vibrational mode and the second-order longitudinal optical (2LO) mode, respectively [32]. The disorder-associated D Raman band gives information on ceria intrinsic defect sites, so the more intense it appears, the higher amount of defect sites will have the analyzed ceria. Additionally, an asymmetric band at 832 cm^{-1} is observed, which corresponds to the O–O stretching vibrations of adsorbed molecular oxygen, suggesting the formation of active

peroxide (O_2^{2-}) species on its surface [32]. The Raman band at $\sim 1075 \text{ cm}^{-1}$ on ceria polycrystals is due to residue nitrate species left from the synthesis process [32] (see band denoted by asterisk in Figure 3b), missing in the Pd/CeO₂ sample because of the involved calcination step. After loading Pd, the disorder-associated band broadens and becomes more intense, and it can be deconvoluted into new defect-induced peaks. A detailed view of this region is given in Figure 3b. As mentioned, the band at 595 cm^{-1} , which from now onwards will be referred to as D₁, is linked to “intrinsic” defects and originates from oxygen vacancies and replacement of Ce^{IV} atoms by reduced Ce^{III} cations [33], although other authors have assigned it to Frenkel-type anion defects, i.e., vacancies created when an oxygen atom moves from its lattice position into an octahedral interstitial position [32,34]. This vibrational feature has been also ascribed to defect spaces, including a dopant cation in 8-fold coordination O²⁻ without any O²⁻ vacancy [35,36], but it will be considered anyway “intrinsic”, i.e., already present in pure ceria structure. In addition to the mentioned D₁ band, an intense D₂ component near 540 cm^{-1} can be detected, attributed to defect spaces involving an oxygen vacancy coupled with Ce^{III} or other aliovalent dopant cations introduced in the ceria lattice [37–39]. Lastly, there is a third D₃ component, centered at 630 cm^{-1} but weaker than the other two, which is probably associated to “extrinsic” defects caused by the addition of dopants. It has been previously assigned to the presence of MO₈ units that do not contain oxygen vacancies, where M is a foreign cation [36,38]. According to the literature, an estimation of the number of defects in the catalyst can be provided through the intensity ratio between the D and the F_{2g} bands. Indeed, various reports claim that the tendency of the catalytic activity for CO and other gas phase oxidation reactions can be well evidenced based on the D/F_{2g} ratio values [40,41]. Although the disorder-associated band clearly broadens and becomes more intense after the Pd loading, D/F_{2g} ratios have been calculated for both as-synthesized samples from their corresponding spectrum, increasing from 0.10 to 0.75 (variation factor of 7.5) upon palladium loading. It is worth noting the presence of an additional peak near 650 cm^{-1} for the Pd/CeO₂ catalyst, which corresponds to the B_{1g} vibrational mode of the Pd–O bond [36,42]. The presence of the latter peak and the new D₃ component could denote a Pd–ceria interaction, possibly entailing the incorporation of some Pd cations into the uppermost ceria layers, without dissolving into the bulk, a fact that could explain the absence of a PdO phase in the XRD pattern. Both Raman spectra show a peak at 350 cm^{-1} and a shoulder near 420 cm^{-1} on the left side of the fluorite band. Although no clear assignment could be found in the literature for these signals, they have been observed for ceria nanoparticles [32,43] and could be attributed to distortion in the lattice [34,38]. The presence of all the mentioned bands, some of them not clearly resolved, represents the heterogeneous environment where a specific defect type can be found.

Summarizing, the incorporation of Pd to the ceria system induces an increase in the amount of the intrinsic defect sites associated with both oxygen vacancies and reduced Ce^{III} atoms, reflected by an intense growth of the D₁ component and the appearance of an intense D₂ band. The presence of the new D₃ component and a band near 650 cm^{-1} suggest a stronger Pd–CeO₂ interaction, possibly involving the incorporation of some Pd cations into the first layers of ceria structure. A variation of lattice parameters caused by Pd incorporation into bulk ceria (with a different atomic radius value) would have been observable in the ceria XRD pattern, which showed no variation upon Pd loading and thus supported the suggested assumptions.

H₂-TPR was used to investigate the reducibility of ceria and Pd/CeO₂ catalysts and the influence of the incorporation of palladium on its redox behavior, and results are reported in Figure 4. It is widely known that reduction of CeO₂ powders occurs at temperatures higher than $400\text{--}500 \text{ }^\circ\text{C}$ [44] and via a stepwise mechanism so that their TPR profiles show a bimodal shape, with a first peak at low temperature attributed to the reduction of the most outer layers of Ce^{IV} (surface reduction) and a large peak at high temperature characteristic of the reduction of the inner Ce^{IV} layers (bulk reduction) [45]. As seen in Figure 4, ceria polycrystals show a first wide peak between $400\text{--}600 \text{ }^\circ\text{C}$, characteristic of surface reduction,

and a major peak around 700 °C, attributed to bulk reduction. The incorporation of Pd on CeO₂ nanocrystals promotes significantly the surface reduction of ceria by spillover from Pd species onto the support, which is reflected with a decrease in this reduction temperature from ca. 450 °C to ca. 370 °C.

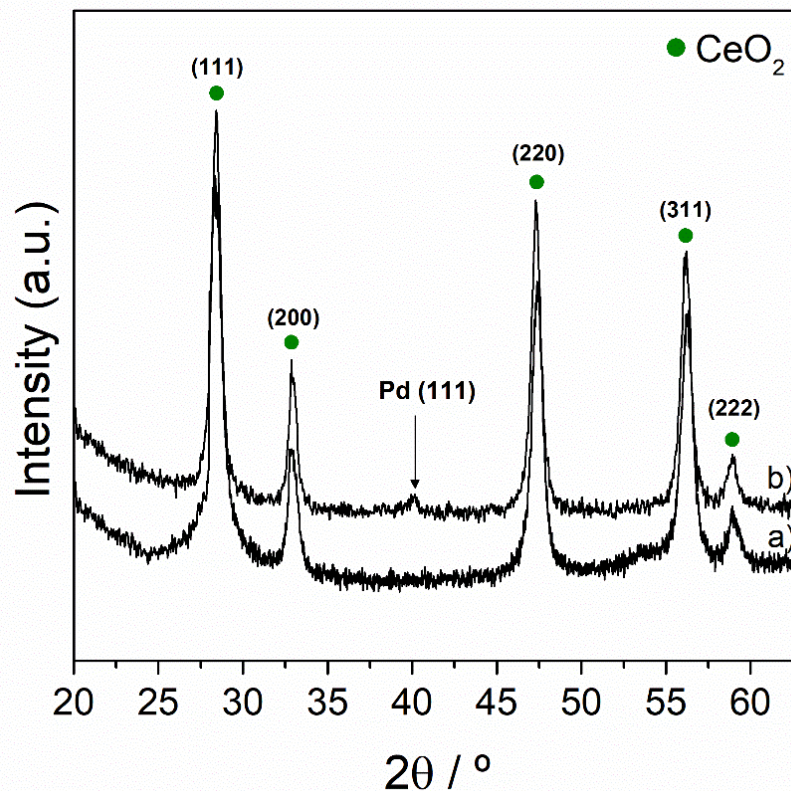


Figure 2. XRD patterns of (a) CeO₂ and (b) Pd/CeO₂ catalysts.

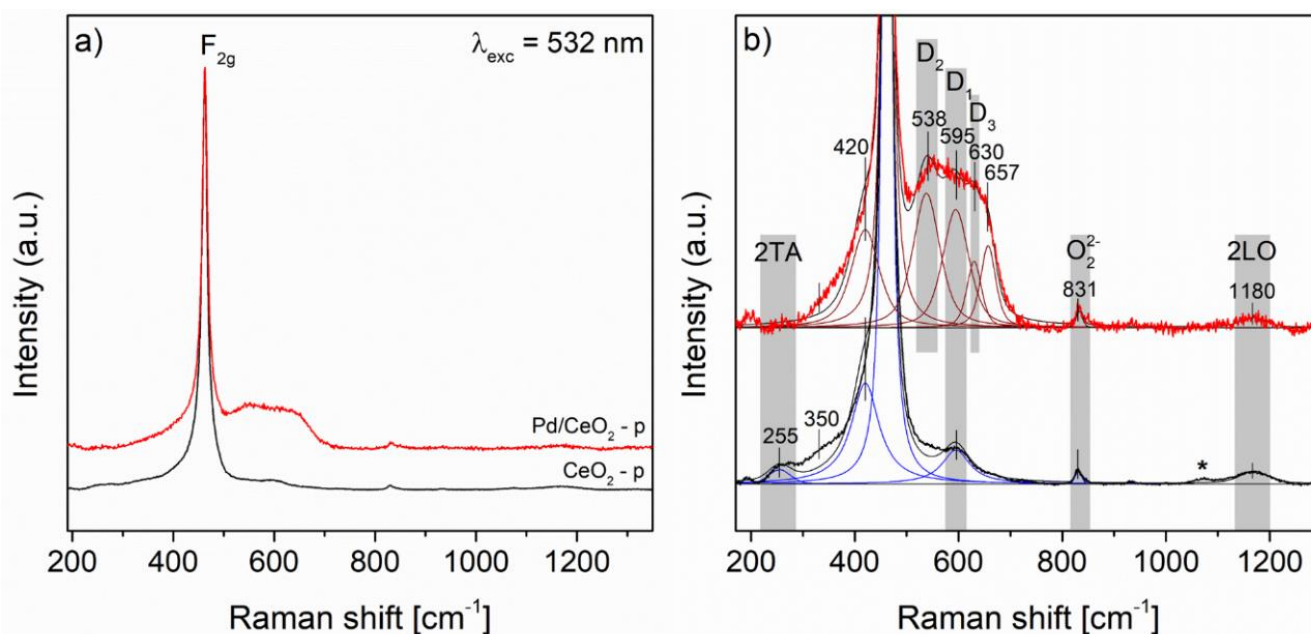


Figure 3. (a) General and (b) detailed views of Raman spectra of ceria polycrystals before and after palladium impregnation. All spectra have been normalized to the F_{2g} peak and vertically shifted for clarity.

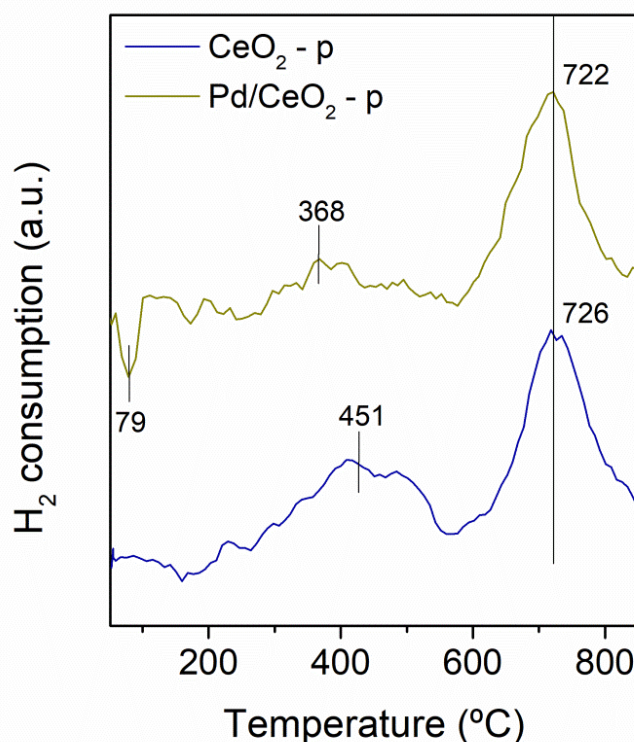


Figure 4. H₂-TPR profiles of CeO₂ support and Pd/CeO₂ powder catalyst.

Interestingly, an additional and negative peak appears near 80 °C, which is commonly assigned to decomposition of the Pd hydride phase that is formed during H₂-TPR at lower temperatures, as already reported [46].

3.2. Operando NAP-XPS

Near ambient pressure X-ray photoelectron spectroscopy was performed to characterize the chemical composition of the surface of both samples during CO oxidation under *operando* conditions by recording the high-resolution spectra of Ce 3d, O 1s, Pd 3d and C 1s photoelectrons. The spectrum corresponding to the Ce 3d core level region is rather complex and can be fitted with 10 peaks, with two and three doublets assigned to Ce^{III} and Ce^{IV} species, respectively. Figure 5a shows a sequence of Ce 3d spectra recorded over Pd/CeO₂ under different experimental conditions. All the contributions are consistent with other literature reports [30,47].

As expected, heating the Pd/CeO₂ catalyst from room temperature to 350 °C under an H₂ rich atmosphere increased the catalyst Ce^{III}/Ce ratio up to a value of 55%, while the introduction of CO (1 mbar) caused a slight decrease in this ratio, down to around 50%. This effect can be observed through a small drop in intensity of the Ce³⁺ V₀, V', U₀, and U' peaks, with binding energies of 880.7, 885.3, 899 and 903.6 eV, respectively. However, the most significant change of the Ce^{III} amount came when introducing O₂ in the subsequent reaction steps (1.5 mbar of CO:O₂ = 2:1), which caused a decrease in the Ce^{III}/Ce ratio down to 25.5% (see Figure 6a) due to the exceptional oxygen storage capacity of ceria, able to capture and accommodate oxygen atoms on its structure in an oxidant environment.

O 1s spectra can be deconvoluted into multiple components due to the presence of oxygen atoms in different coordination environments [48]. Although the interpretation of the different contributions is complex due to the proximity between the components present, changes in the cerium oxidation state are consistent enough comparing the Ce 3d (Figure 5a) with the O 1s spectra (Figure 5b) recorded under the same experimental conditions, as illustrated in Figure 6a. For the impregnated catalyst, the component at lower binding energy (528.4 eV) corresponds to the oxygen atoms bonded to Ce^{IV}, while the con-

tribution appearing approximately at 529.9 eV is here related to three-fold oxygen (oxygen atoms bonded to Ce^{III} or near to oxygen vacancies). Finally, the shoulder at 532 eV can be attributed to surface hydroxyl groups, likely due to the interaction with H_2 gas during the pre-treatment step. It is worth mentioning that the Pd $3p_{3/2}$ contribution, centered at 532.4 and 534.2 eV for metallic palladium and PdO, respectively [49,50], significantly overlaps with O 1s bands. Nevertheless, its signal ought to be much less intense with respect to the corresponding Pd 3d component, a fact that supports the rejection of this such possible contribution. The injection of CO into the analysis chamber resulted in the appearance of its characteristic gas phase band between 536–537 eV [51], emphasizing the powerful capabilities of the NAP-XPS technique that, in addition to the sample surface composition, can also detect the gas molecules surrounding the sample. It is worth mentioning that the position of gas phase species can slightly vary depending on the work function of the sample surface. For this reason, CO contribution appears at lower B_E upon O_2 injection. Two additional peaks at 537.4 and 538.5 eV appeared when dosing oxygen (denoted by red asterisks in Figure 5a), and correspond to contributions of O_2 from the gas phase [51]. CO species can also be confirmed through C 1s spectra (see spectrum ii from Figure 7), where a new feature around 291 eV was observed in addition to the C 1s signal at 284.8 eV, typically assigned to C–C bonds of amorphous carbon contamination [52]. Another contribution could be discerned at 285.6 eV, most probably indicating an interaction of CO molecules with Pd, as will be discussed thereafter.

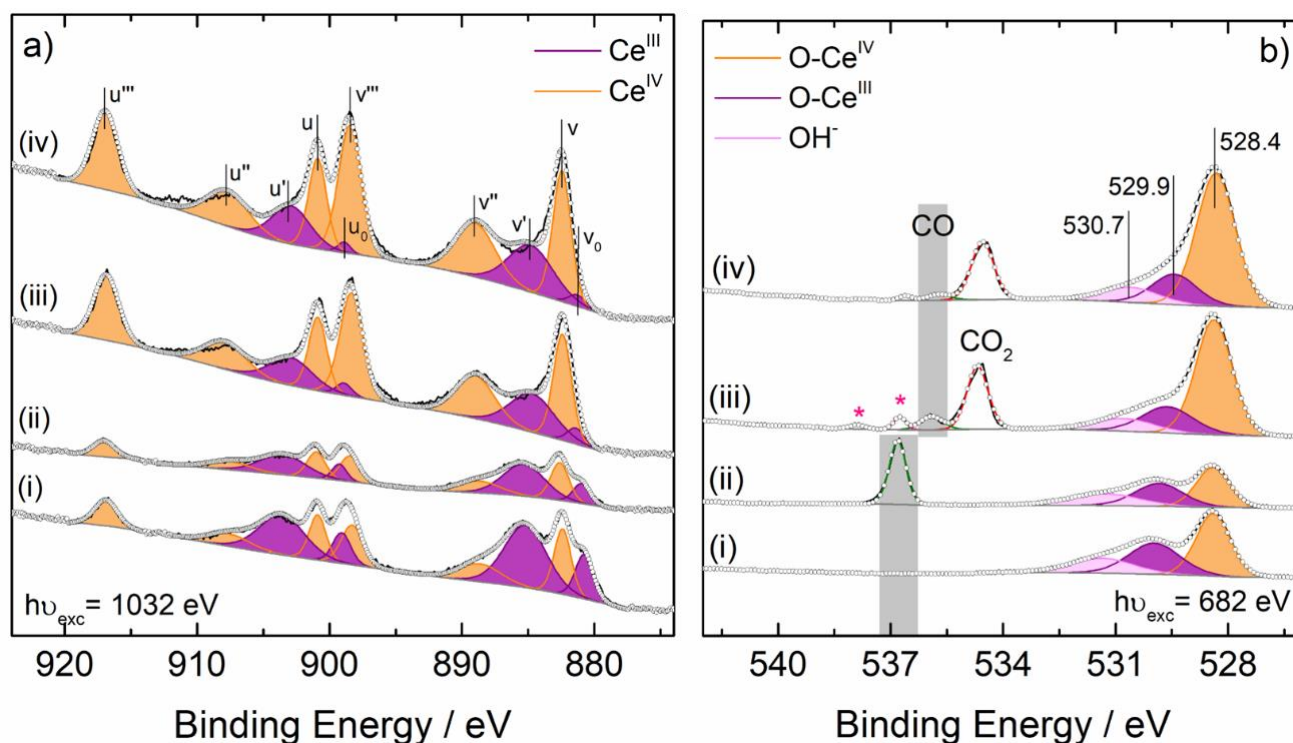


Figure 5. (a) Operando XPS spectra of Ce 3d and (b) O 1s recorded over Pd/CeO₂ catalyst under the following conditions: (i) reduction under 1 mbar of H₂ at 350 °C, (ii) 1 mbar pressure of CO at 250 °C, (iii) CO oxidation under 1.5 mbar total pressure of CO:O₂ = 2:1 at 250 °C, and (iv) CO oxidation under 1.5 mbar total pressure of CO+O₂ at 350 °C.

Similarly, after the exposure to O_2 , a new band at 534.5 eV demonstrated the presence of gaseous CO_2 generated through CO oxidation, as displayed in Figure 5b. Indeed, carbon dioxide was immediately formed as a reaction product and its presence could be again proved through both O 1s and C 1s spectra. As observed in Figure 7 (spectrum iii), O_2 oxidized all the existing carbonaceous species, and the characteristic peak of adventitious carbon at 284.8 eV disappeared while an intense band near 293 eV was simultaneously

detected next to the CO signal, which is assigned to carbon dioxide gas phase. The presence of carbon dioxide was also confirmed by mass spectroscopy. Figure 6b shows the evolution of O₂, CO and CO₂ partial pressures inside the analysis chamber, recorded by means of a quadrupole mass spectrometer, located in the second stage of the differential pumping system of the NAP-XPS analyzer, which probes the gases flowing from the proximity of the sample surface towards the detector. The shaded areas depict the three different atmospheres (H₂, CO and CO + O₂) generated for the sequence of experiments studied, and a clear variation took place upon O₂ injection, as CO₂ partial pressure rapidly increased at the expense of CO and O₂ consumption by the oxidation reaction.

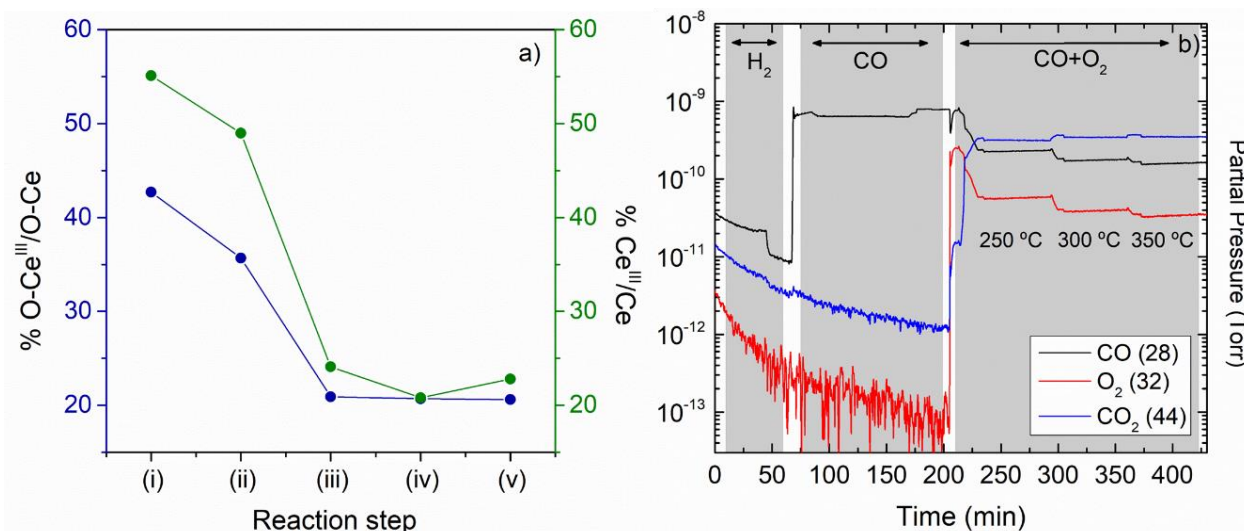


Figure 6. (a) Amount of reduced ceria measured at each reaction step from O 1s spectra at 682 eV (left axis) and Ce 3d spectra at 1032 eV (right axis) of the Pd/CeO₂ catalyst and (b) corresponding partial pressures of O₂, CO and CO₂ monitored by mass spectroscopy.

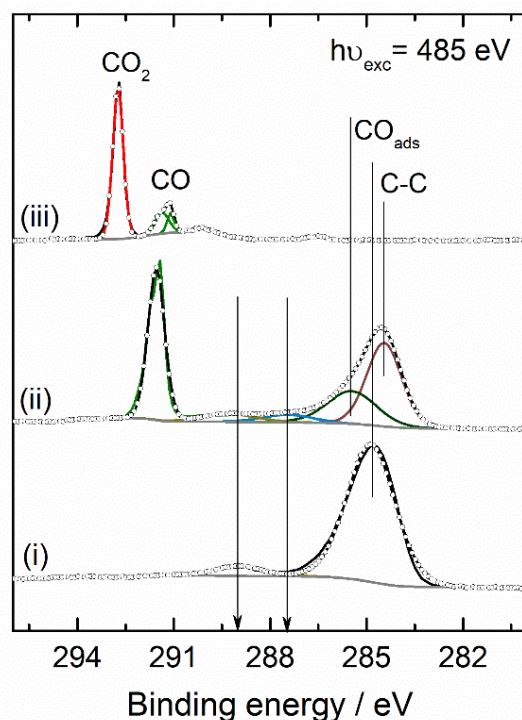


Figure 7. Operando XPS spectra of C 1s recorded over Pd/CeO₂ catalyst during CO oxidation under the following conditions: (i) reduction under 1 mbar of H₂ at 350 °C, (ii) 1 mbar pressure of CO at 250 °C, and (iii) CO oxidation under 1.5 mbar total pressure of CO:O₂ = 2:1 at 250 °C.

Figure 8 shows the Pd 3d spectra of the Pd/CeO₂ catalyst, which displayed interesting variations of its oxidation states during the different reaction steps. Under H₂ atmosphere, palladium appeared completely reduced, with its Pd 3d_{5/2} and Pd 3d_{3/2} signals centered at 335.5 and 341 eV, respectively. The position of these signals did not substantially vary upon changing the initial atmosphere for CO, but the asymmetric line shape typical of metallic-like Pd was slightly lost, indicating the presence of an intermediate-B_E component at approximately 336 eV. According to the literature, the latter value is centered between the typical positions of bulk Pd metal ($B_E(\text{Pd}3d_{5/2}) = 335.2 \pm 0.2$ eV) and bulk PdO ($B_E(\text{Pd}3d_{5/2}) = 336.8 \pm 0.2$ eV) [53], and it cannot be attributed to the PdO phase since the characteristic shake-up satellites of the oxide near 341 and 346 eV are not observed in the XP spectra [54]. This component could be assigned to chemisorbed CO molecules but, according to the literature, it could also be attributed to small semi-oxidized palladium clusters, denoting them as PdO_x [19,55,56], that could be formed at the upper atomic layers of Pd-based catalysts by CO dissociation. Indeed, the shift of the photoelectron lines towards higher binding energies (with respect to the typical value of the palladium metal state, $B_E(\text{Pd}3d_{5/2}) = 334.8 - 335.4$ eV) can be explained by the size effects during the photoionization process of metal clusters. When the size of metal clusters deposited on insulating supports is reduced, the extra-atomic relaxation and charge conservation in the final state is not as effective as for larger particles or bulk samples. In other words, Pd atoms of the cluster boundaries are subjected to an intense polarizing effect from ceria lattice oxygen atoms, which can lead to the transfer of some electron density to the support and, consequently, to the formation of partially charged palladium atoms with an oxidation state value between Pd⁰ and Pd^{II} [19,55]. The ratio between boundary and the total number of Pd atoms in the cluster raises as its dimensions decrease, so that small Pd clusters probably include a greater number of Pd–O bonds than Pd–Pd ones, modifying the chemical shift of Pd photoelectron lines. For this reason, this state has been referred to as PdO_x, considering both possibilities, i.e., the interaction with adsorbed CO molecules on Pd [57] and the formation of clusters due to CO dissociation reported in the literature, indicating an oxidation state between Pd⁰ and Pd^{II}. As the component centered at 336 eV appeared with the injection of CO, it could be attributed to the formation of palladium carbide (PdC) surface species [58–60], also reported under CO environments by dissociation of part of the CO molecules adsorbed on surface metallic Pd and transient storage of atomic carbon within the palladium nanoparticles, thus generating PdC [59,60]. Nevertheless, no equivalent PdC species peak could be identified in the C 1s core-level spectrum obtained in CO atmosphere (see spectrum ii of Figure 7), usually centered at 283.7 eV. As observed in spectrum ii of Figure 7, a peak at 285.5 eV indicated the interaction of CO with the catalyst surface, attributed to CO molecules adsorbed in hollow/bridge sites on the metallic Pd surface [61,62]. Arrows in Figure 7 indicate two other weak features around 287.4 and 289 eV in C 1s spectra, attributed to oxygen-containing species residing on the surface, specifically assigned to C=O and O=C–O groups [63]. As observed in Figure 8b, the fraction of the PdO_x phase was reduced by more than half (from a value of 74% to 28%) when O₂ was added to CO at 250 °C. Simultaneously, the introduction of O₂ gave rise to the formation of a different Pd species with intense bands at 338.1 and 343.4 eV (Pd3d_{5/2} and Pd3d_{3/2} respectively, see Figure 8). This Pd3d_{5/2} value exceeds by far the typical B_E value of PdO (336.8 ± 0.2 eV), and it could be attributed to the formation of the most oxidized palladium state (IV) [64] or fine PdO nanoparticles with low-coordinated Pd^{II} ions [65]. Nevertheless, the B_E(Pd3d_{5/2}) values for all PdO species are in the range of 336.0–337.2 eV and PdO₂ compounds are known to be unstable powerful oxidants [65,66]. Therefore, this increased B_E(Pd3d_{5/2}) value can be explained by the presence of Pd^{II} cations in an environment different from the PdO crystalline matrix, or palladium atoms with a chemical state of Pd^{δ+} (2 < δ ≤ 4). Actually, Pd/CeO₂ catalysts habitually exhibit such an elevated value of B_E(Pd3d_{5/2}) [19,23,24,67,68], and multiple studies have attributed it to Pd^{II} cations in the matrix of a Pd_xCe_{1-x}O_{2-δ} solution at the surface layers of the ceria lattice, possibly coordinated to four oxygen ions to form a near square-planar geometry [22–24,42,56]. Thus,

the positive shift of the Pd3d_{5/2} line is ascribed to a decrease in Pd–O distances generated in the Pd_xCe_{1-x}O_{2-δ} solution [24,42].

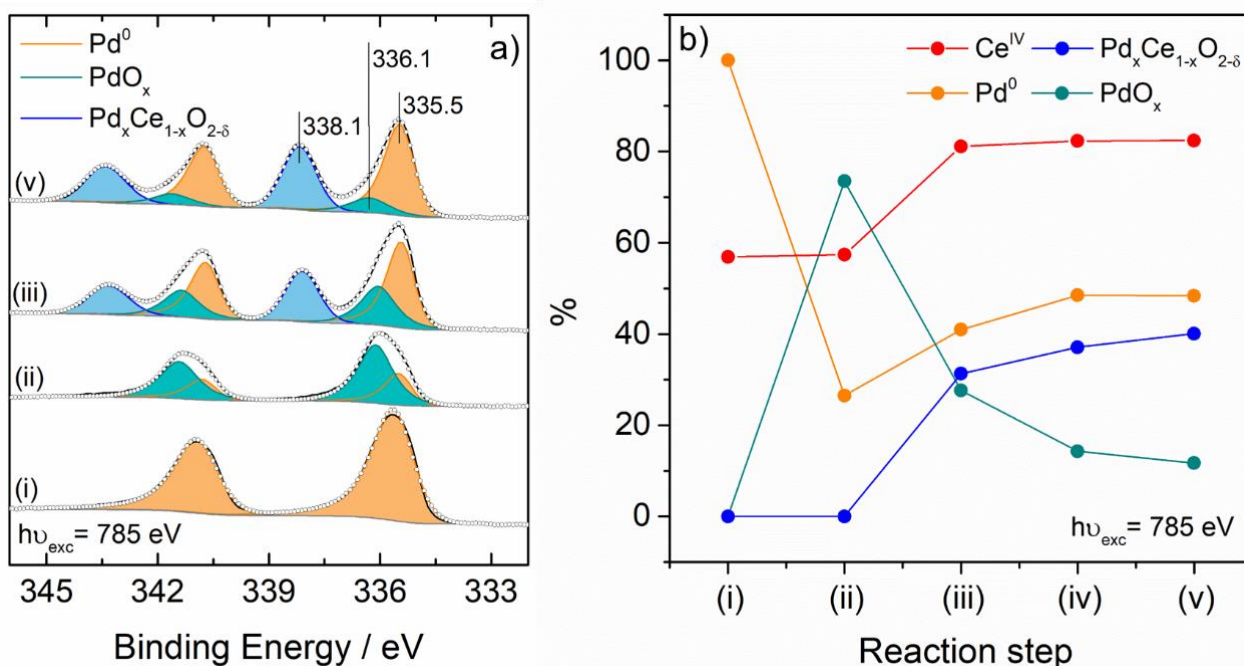


Figure 8. (a) Operando Pd 3d XPS spectra recorded at a photon energy of 785 eV over Pd/CeO₂ catalyst under the following conditions: (i) reduction under 1 mbar of H₂ at 350 °C, (ii) 1 mbar pressure of CO at 250 °C, (iii) CO oxidation under 1.5 mbar total pressure of CO:O₂ = 2:1 at 250 °C, and (v) CO oxidation under 1.5 mbar total pressure of CO + O₂ at 350 °C; (b) amount of reduced and oxidized Pd and Ce species measured at each reaction step from Pd 3d (785 eV) and Ce 3d (1332 eV) spectra of the Pd/CeO₂ catalyst. The use of these excitation energies allows an analysis of comparable probing depths, i.e., acquiring Pd and Ce photoelectrons with ~450 eV.

Interestingly, CO oxidation took place with the appearance of this active Pd_xCe_{1-x}O_{2-δ} phase, which in turn was generated at the expense of the PdO_x species upon dosing gaseous oxygen at 250 °C. Additionally, an increase in the temperature under the reaction mixture led to a gradual decrease in the PdO_x amount and a simultaneous rise in the Pd_xCe_{1-x}O_{2-δ} solution phase, indicated by an intense growth of the component at 338.1 eV (Figure 8a). It is not clear whether the PdO_x phase contributes to the CO oxidation nor to what extent it does so, but three Pd phases were observed through the Pd 3d spectra of the catalyst under reaction mixture, most probably due to being the Pd_xCe_{1-x}O_{2-δ} phase, the active form for Pd. A non-destructive depth profile analysis using variable synchrotron excitation energies was performed to elucidate the location and, consequently, the nature and role of these palladium phases in the CO oxidation reaction, and the corresponding Pd 3d spectra are displayed in Figure 9a. Indeed, the use of a lower photon energy, i.e., 485 eV, allows probing of the outermost layers of the sample, since the spectrum obtained at this energy includes Pd 3d photoelectrons with lower kinetic energy, excited from a smaller volume of the sample (more surface-focused) than when the latter is irradiated with 785 eV energy. As observed in Figure 9, the PdO_x component at 336 eV appeared significantly more intense under CO atmosphere (79 vs. 73 %, respectively), suggesting a predominance of such species on the upper surface layers of the metallic Pd supported nanoparticles. The amount of PdO_x phase gradually decreased under reaction mixture and increasing temperature, but at 350 °C PdO_x species were more abundant in the subsurface than in the uppermost surface layers of the catalyst. From such behavior it could be deduced that, although the active form of Pd is the surface Pd_xCe_{1-x}O_{2-δ} phase, PdO_x species also play a role on CO oxidation evolution and its consumption (especially at the surface of the catalyst, in

contact with the gaseous reactants) is directly related to the appearance and stabilization of the active $\text{Pd}_x\text{Ce}_{1-x}\text{O}_{2-\delta}$ phase. Nevertheless, CO_2 formation has been mainly attributed to the generation of the active $\text{Pd}_x\text{Ce}_{1-x}\text{O}_{2-\delta}$ phase [56,69], which clearly appeared at the Pd– CeO_2 interface in contact with the environment, that is, at the Pd nanoparticle boundaries exposed to both ceria support and gas environment. As observed in Figure 9b, the amount of $\text{Pd}_x\text{Ce}_{1-x}\text{O}_{2-\delta}$ solution phase exceeded the amount of remaining metallic palladium (49 vs. 43%, respectively) under an atmosphere of $\text{CO}:\text{O}_2 = 2:1$ at 350°C , as opposed to the subsurface of the catalyst (see Figure 8b), where Pd^0 species still prevailed over the other oxidation states (48 vs. 40%, respectively).

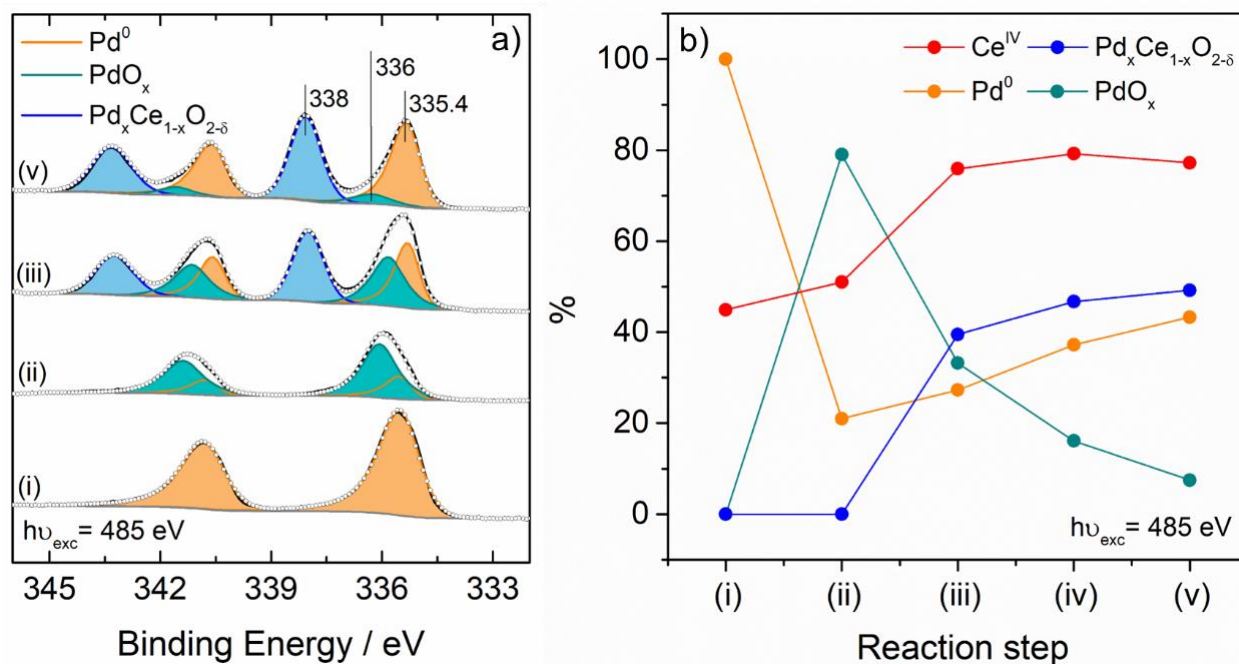


Figure 9. (a) *Operando* Pd 3d XPS spectra recorded at a photon energy of 485 eV over Pd/ CeO_2 catalyst under the following conditions: (i) reduction under 1 mbar of H_2 at 350°C , (ii) 1 mbar pressure of CO at 250°C , (iii) CO oxidation under 1.5 mbar total pressure of $\text{CO}:\text{O}_2 = 2:1$ at 250°C , and (v) CO oxidation under 1.5 mbar total pressure of $\text{CO} + \text{O}_2$ at 350°C ; (b) amount of reduced and oxidized Pd and Ce species measured at each reaction step from Pd 3d (485 eV) and Ce 3d (1032 eV) spectra of the Pd/ CeO_2 catalyst. The use of these excitation energies allows an analysis of comparable probing depths, i.e., acquiring Pd and Ce photoelectrons with $\sim 150 \text{ eV}$.

As already stated, CO oxidation proceeds through the Mars–van Krevelen mechanism over reducible oxide supported metal NP catalysts [10], where lattice oxygen atoms of the ceria surface are transferred to CO_{ads} , and gaseous oxygen subsequently fills the created vacancies on the oxide. From an electron transfer point of view, CO oxidation process is based on the electron transfer from CO_{ads} to the catalyst and then to O_2 , but the contribution of the palladium phase cannot be ignored in such supported catalytic system. An electron transfer model which correlates electronic Pd– CeO_2 interactions and the Mars–van Krevelen mechanism in CO oxidation was confirmed by Zhao et al. by means of density functional theory calculations [70]. As proposed on Tang’s work [71], the electron transfer occurring at the Pd/ CeO_2 interface starts with the creation of surface active oxygen species when the reduced Ce^{III} is exposed to molecular O_2 and transfers electrons to it, also generating Ce^{IV} species (Equation (2)). Those active oxygen species then spillover onto the CO molecules adsorbed on Pd^{II} active sites to produce CO_2 (Equation (3)) and an oxygen vacancy associated with two electrons left, which reduce palladium to its metallic state. Those electrons are eventually transferred from Pd^0 to Ce^{IV} species to obtain again active

Pd^{II} and Ce^{III} ($\text{Pd}^0 + 2\text{Ce}^{\text{IV}} \rightarrow \text{Pd}^{\text{II}} + 2\text{Ce}^{\text{III}}$), and thus close the electron transfer cycle from CO_{ads} to the catalyst and ultimately to O_2 , as illustrated in the scheme of Figure 10.

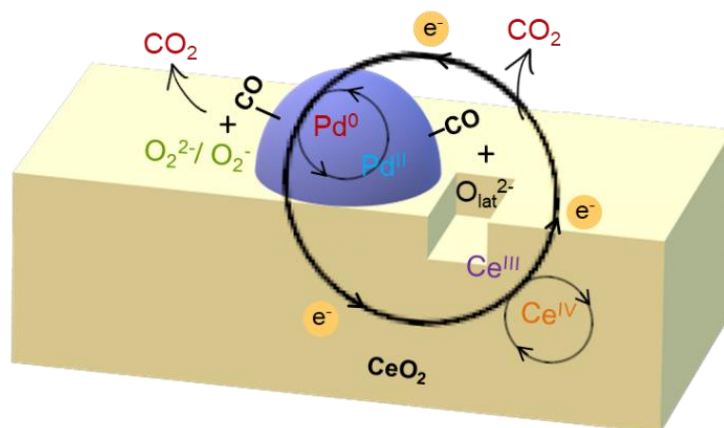


Figure 10. Illustrative scheme of the suggested electron transfer model for the CO oxidation reaction occurring on the Pd/CeO₂ surface catalyst.

All in all, our results indicate that a PdO_x phase is formed in the presence of CO, which could be somehow related to the appearance of the active Pd_xCe_{1-x}O_{2-δ} phase upon introducing O₂. The obtained in situ data should be beneficial and taken into consideration for a full theoretical understanding of the CO oxidation over oxide-supported palladium nanoparticles. The comparison of the presented results with *operando* NAP-XPS measurements of the Pd/CeO₂ system in other conditions, such as under O₂ at lower temperatures, followed by an atmosphere of CO and, subsequently, a mixture of gaseous CO + O₂, would be certainly helpful to understand both the surface and the subsurface dynamics and thus further elucidate the mechanism of CO oxidation on the Pd/CeO₂ system.

4. Conclusions

This work examines the CO oxidation reaction by *operando* NAP-XPS on a Pd/CeO₂ powder catalyst prepared by conventional incipient wetness impregnation. SEM, HRTEM and XRD analyses revealed uniformly CeO₂-loaded Pd nanoparticles of less than 2 nm, which generated an increase in oxygen vacancies with concomitant ceria reduction, as indicated by H₂-TPR and Raman measurements. The presence of adsorbed peroxide (O₂²⁻) species on the catalyst surface could also be demonstrated by Raman spectra. *Operando* NAP-XPS measurements revealed two kinds of surface palladium species under reaction conditions, consisting of electropositive Pd atoms forming a PdO_x phase located at the upper surface layers of the metallic Pd supported NPs, and Pd^{II} ions interacting with the surface ceria fluorite structure as a Pd_xCe_{1-x}O_{2-δ} solution, created at the Pd–CeO₂ interface in contact with the gas environment. The formation of PdO_x took place under a CO atmosphere, most probably by CO dissociation on surface metallic Pd atoms, and the surface Pd_xCe_{1-x}O_{2-δ} phase was instantly generated upon injecting gaseous O₂ in the CO environment, becoming the predominant surface species (49.2% at 485 eV) at 350 °C under reaction mixture. The latter species appeared to be very active, and thus crucial, for CO oxidation, acting as a route through which active oxygen species could be transferred from ceria to Pd species for CO oxidation. This work demonstrates the importance of the surface and subsurface chemistry in oxidation processes by *operando* NAP-XPS measurements.

Author Contributions: X.G.: Writing—Original Draft Preparation, Formal analysis, Investigation, Visualization; L.S.: Investigation; X.V.: Investigation; I.S.: Investigation; F.H.: Investigation; J.P.: Investigation; E.S.: Investigation; M.T.: Investigation; J.L.: Conceptualization, Investigation Writing—Review & Editing, Supervision, Project administration, Funding acquisition; C.E.: Conceptualization, Investigation Writing—Review & Editing, Supervision, Project administration, Funding acquisition. All authors have read and agreed to the published version of the manuscript.

Funding: Ministerio de Ciencia e Innovación: MICINN/FEDER PID2021-124572OB-C31, PID2021-124572OB-C33; Severo Ochoa FUNFUTURE: CEX2019-000917-S; Generalitat de Catalunya: FI-DGR 2017 00137; MICINN Ramon y Cajal: RYC2019-026704-I; Generalitat de Catalunya for Beatriu de Pinós: 2017-BP-00020.

Acknowledgments: This research has been funded by projects MICINN/FEDER PID2021-124572OB-C31, PID2021-124572OB-C33, Severo Ochoa FUNFUTURE (CEX2019-000917-S) and GC 2017 SGR 128. X.G. is grateful to Generalitat de Catalunya for grant FI-DGR 2017 00137. J.L. is a Serra Hünter Fellow and is grateful to ICREA Academia program. L.S. is grateful to MICINN Ramon y Cajal program for an individual fellowship grant agreement RYC2019-026704-I. XV thanks the Generalitat de Catalunya for a Beatriu de Pinós fellowship, grant agreement No 2017-BP-00020. F.C.H. acknowledges the Argentinian National Research Council (CONICET) for the financial support. We also thank the ALBA synchrotron staff for the successful performance of the CIRCE beamline during the NAP-XPS experiments and T. Trifonov for technical assistance.

Conflicts of Interest: The authors declare no conflict of interest.

References

1. Aneggi, E.; Boaro, M.; de Leitenburg, C.; Dolcetti, G.; Trovarelli, A. Insights into the redox properties of ceria-based oxides and their implications in catalysis. *J. Alloys Compd.* **2006**, *412*, 1096–1102. [[CrossRef](#)]
2. Vivier, L.; Duprez, D. Ceria-Based Solid Catalysts for Organic Chemistry. *ChemSusChem* **2010**, *3*, 654–678. [[CrossRef](#)] [[PubMed](#)]
3. Bueno-López, A.; Krishna, K.; Makkee, M.; Moulijn, J.A. Active oxygen from CeO₂ and its role in catalysed soot oxidation. *Catal. Lett.* **2005**, *99*, 203–205. [[CrossRef](#)]
4. Freund, H.-J.; Meijer, G.; Scheffler, M.; Schlögl, R.; Wolf, M. CO Oxidation as a Prototypical Reaction for Heterogeneous Processes. *Angew. Chem. Int. Ed.* **2011**, *50*, 10064–10094. [[CrossRef](#)]
5. Montini, T.; Melchionna, M.; Monai, M.; Fornasiero, P. Fundamentals and Catalytic Applications of CeO₂-Based Materials. *Chem. Rev.* **2016**, *116*, 5987–6041. [[CrossRef](#)]
6. Trovarelli, A.; de Leitenburg, C.; Boaro, M.; Dolcetti, G. The utilization of ceria in industrial catalysis. *Catal. Today* **1999**, *50*, 353–367. [[CrossRef](#)]
7. Kim, G. Ceria-promoted three-way catalysts for auto exhaust emission control. *Ind. Eng. Chem. Prod. Res. Dev.* **1982**, *21*, 267–274. [[CrossRef](#)]
8. Kaspar, J.; Fornasiero, P.; Balducci, G.; Di Monte, R.; Hickey, N.; Sergo, V. Effect of ZrO₂ content on textural and structural properties of CeO₂-ZrO₂ solid solutions made by citrate complexation route. *Inorg. Chim. Acta* **2003**, *349*, 217–226. [[CrossRef](#)]
9. Sun, C.; Li, H.; Chen, L. Nanostructured ceria-based materials: Synthesis, properties, and applications. *Energy Environ. Sci.* **2012**, *5*, 8475–8505. [[CrossRef](#)]
10. Bueno-Loópez, A.; Krishna, K.; Makkee, M.; Moulijn, J.A. Enhanced soot oxidation by lattice oxygen via La³⁺-doped CeO₂. *J. Catal.* **2005**, *230*, 237–248. [[CrossRef](#)]
11. Soler, L.; Casanovas, A.; Escudero, C.; Pérez-Dieste, V.; Aneggi, E.; Trovarelli, A.; Llorca, J. Ambient Pressure Photoemission Spectroscopy Reveals the Mechanism of Carbon Soot Oxidation in Ceria-Based Catalysts. *ChemCatChem* **2016**, *8*, 2748–2751. [[CrossRef](#)]
12. Slavinskaya, E.M.; Boronin, A.I.; Danilova, I.G.; Amosov, Y.I.; Ivanova, A.S.; Kuznetsov, P.A.; Polukhina, I.A.; Gulyaev, R.V.; Stadnichenko, A.I.; Koshcheev, S.V.; et al. Synthesis and physicochemical characterization of palladium-cerium oxide catalysts for the low-temperature oxidation of carbon monoxide. *Kinet. Catal.* **2009**, *50*, 819–823. [[CrossRef](#)]
13. Bunluesin, T.; Gorte, R.; Graham, G. Studies of the water-gas-shift reaction on ceria-supported Pt, Pd, and Rh: Implications for oxygen-storage properties. *Appl. Catal. B Environ.* **1998**, *15*, 107–114. [[CrossRef](#)]
14. Hilaire, S.; Wang, X.; Luo, T.; Gorte, R.; Wagner, J. A comparative study of water-gas-shift reaction over ceria supported metallic catalysts. *Appl. Catal. A Gen.* **2001**, *215*, 271–278. [[CrossRef](#)]
15. Ramírez-López, R.; Elizalde-Martínez, I.; Balderas-Tapia, L. Complete catalytic oxidation of methane over Pd/CeO₂-Al₂O₃: The influence of different ceria loading. *Catal. Today* **2010**, *150*, 358–362. [[CrossRef](#)]
16. Rossell, M.D.; Caparrós, F.J.; Angurell, I.; Muller, G.; Llorca, J.; Seco, M.; Rossell, O. Magnetite-supported palladium single-atoms do not catalyse the hydrogenation of alkenes but small clusters do. *Catal. Sci. Technol.* **2016**, *6*, 4081–4085. [[CrossRef](#)]
17. Nagai, Y.; Hirabayashi, T.; Dohmae, K.; Takagi, N.; Minami, T.; Shinjoh, H.; Matsumoto, S.I. Sintering inhibition mechanism of platinum supported on ceria-based oxide and Pt-oxide-support interaction. *J. Catal.* **2006**, *242*, 103–109. [[CrossRef](#)]

18. Hu, Z.; Liu, X.; Meng, D.; Guo, Y.; Guo, Y.; Lu, G. Effect of Ceria Crystal Plane on the Physicochemical and Catalytic Properties of Pd/Ceria for CO and Propane Oxidation. *ACS Catal.* **2016**, *6*, 2265–2279. [[CrossRef](#)]
19. Boronin, A.; Slavinskaya, E.; Danilova, I.; Gulyaev, R.; Amosov, Y.; Kuznetsov, P.; Polukhina, I.; Koscheev, S.; Zaikovskii, V.; Noskov, A. Investigation of palladium interaction with cerium oxide and its state in catalysts for low-temperature CO oxidation. *Catal. Today* **2009**, *144*, 201–211. [[CrossRef](#)]
20. Mayernick, A.D.; Janik, M.J. *Ab initio* thermodynamic evaluation of Pd atom interaction with CeO₂ surfaces. *J. Chem. Phys.* **2009**, *131*, 084701. [[CrossRef](#)]
21. Yang, Z.; Luo, G.; Lu, Z.; Hermansson, K. Oxygen vacancy formation energy in Pd-doped ceria: A DFT+U study. *J. Chem. Phys.* **2007**, *127*, 074704. [[CrossRef](#)] [[PubMed](#)]
22. Colussi, S.; Gayen, A.; Camellone, M.F.; Boaro, M.; Llorca, J.; Fabris, S.; Trovarelli, A. Nanofaceted Pd-O Sites in Pd-Ce Surface Superstructures: Enhanced Activity in Catalytic Combustion of Methane. *Angew. Chem. Int. Ed.* **2009**, *48*, 8481–8484. [[CrossRef](#)] [[PubMed](#)]
23. Priolkar, K.R.; Bera, P.; Sarode, P.R.; Hegde, M.S.; Emura, S.; Kumashiro, R.; Lalla, N.P. Formation of Ce_{1-x}Pd_xO_{2-δ} Solid Solution in Combustion-Synthesized Pd/CeO₂ Catalyst: XRD, XPS, and EXAFS Investigation. *Chem. Mater.* **2002**, *14*, 2120–2128. [[CrossRef](#)]
24. Gulyaev, R.; Stadnichenko, A.; Slavinskaya, E.; Ivanova, A.; Koscheev, S.; Boronin, A. In situ preparation and investigation of Pd/CeO₂ catalysts for the low-temperature oxidation of CO. *Appl. Catal. A Gen.* **2012**, *439–440*, 41–50. [[CrossRef](#)]
25. Pérez-Dieste, V.; Aballe, L.; Ferrer, S.; Nicolas, J.; Escudero, C.; Milán, A.; Pellegrin, E. Near Ambient Pressure XPS at ALBA. *J. Phys. Conf. Ser.* **2013**, *425*, 072023. [[CrossRef](#)]
26. Garcia, X.; Soler, L.; Divins, N.J.; Vendrell, X.; Serrano, I.; Lucentini, I.; Prat, J.; Solano, E.; Tallarida, M.; Escudero, C.; et al. Ceria-Based Catalysts Studied by Near Ambient Pressure X-ray Photoelectron Spectroscopy: A Review. *Catalysts* **2020**, *10*, 286. [[CrossRef](#)]
27. Colussi, S.; Trovarelli, A.; Vesselli, E.; Baraldi, A.; Comelli, G.; Groppi, G.; Llorca, J. Structure and morphology of Pd/Al₂O₃ and Pd/CeO₂/Al₂O₃ combustion catalysts in Pd–PdO transformation hysteresis. *Appl. Catal. A Gen.* **2010**, *390*, 1–10. [[CrossRef](#)]
28. Mai, H.-X.; Sun, L.-D.; Zhang, Y.-W.; Si, R.; Feng, W.; Zhang, H.-P.; Liu, A.H.-C.; Yan, C.-H. Shape-Selective Synthesis and Oxygen Storage Behavior of Ceria Nanopolyhedra, Nanorods, and Nanocubes. *J. Phys. Chem. B* **2005**, *109*, 24380–24385. [[CrossRef](#)]
29. Soler, L.; Casanovas, A.; Urrich, A.; Angurell, I.; Llorca, J. CO oxidation and COPrO_x over preformed Au nanoparticles supported over nanoshaped CeO₂. *Appl. Catal. B Environ.* **2016**, *197*, 47–55. [[CrossRef](#)]
30. Mullins, D.; Overbury, S.; Huntley, D. Electron spectroscopy of single crystal and polycrystalline cerium oxide surfaces. *Surf. Sci.* **1998**, *409*, 307–319. [[CrossRef](#)]
31. Päiväsaari, J.; Putkonen, M.; Niinistö, L. Cerium dioxide buffer layers at low temperature by atomic layer deposition. *J. Mater. Chem.* **2002**, *12*, 1828–1832. [[CrossRef](#)]
32. Wu, Z.; Li, M.; Howe, J.; Meyer, I.H.M.; Overbury, S.H. Probing Defect Sites on CeO₂ Nanocrystals with Well-Defined Surface Planes by Raman Spectroscopy and O₂ Adsorption. *Langmuir* **2010**, *26*, 16595–16606. [[CrossRef](#)] [[PubMed](#)]
33. Filtschew, A.; Hofmann, K.; Hess, C. Ceria and Its Defect Structure: New Insights from a Combined Spectroscopic Approach. *J. Phys. Chem. C* **2016**, *120*, 6694–6703. [[CrossRef](#)]
34. Agarwal, S.; Zhu, X.; Hensen, E.J.M.; Lefferts, L.; Mojet, B.L. Defect Chemistry of Ceria Nanorods. *J. Phys. Chem. C* **2014**, *118*, 4131–4142. [[CrossRef](#)]
35. Taniguchi, T.; Watanabe, T.; Sugiyama, N.; Subramani, A.K.; Wagata, H.; Matsushita, N.; Yoshimura, M. Identifying Defects in Ceria-Based Nanocrystals by UV Resonance Raman Spectroscopy. *J. Phys. Chem. C* **2009**, *113*, 19789–19793. [[CrossRef](#)]
36. Li, L.; Chen, F.; Lu, J.-Q.; Luo, M.-F. Study of Defect Sites in Ce_{1-x}M_xO_{2-δ} (x = 0.2) Solid Solutions Using Raman Spectroscopy. *J. Phys. Chem. A* **2011**, *115*, 7972–7977. [[CrossRef](#)]
37. Lin, H.-L.; Wu, C.-Y.; Chiang, R.-K. Facile synthesis of CeO₂ nanoplates and nanorods by [100] oriented growth. *J. Colloid Interface Sci.* **2010**, *341*, 12–17. [[CrossRef](#)]
38. Sartoretti, E.; Novara, C.; Giorgis, F.; Piumetti, M.; Bensaid, S.; Russo, N.; Fino, D. In situ Raman analyses of the soot oxidation reaction over nanostructured ceria-based catalysts. *Sci. Rep.* **2019**, *9*, 3875. [[CrossRef](#)]
39. Paunović, N.; Dohčević-Mitrović, Z.; Scurtu, R.; Aškrabić, S.; Prekajski, M.; Matović, B.; Popović, Z.V. Suppression of inherent ferromagnetism in Pr-doped CeO₂ nanocrystals. *Nanoscale* **2012**, *4*, 5469–5476. [[CrossRef](#)]
40. Piumetti, M.; Andana, T.; Bensaid, S.; Russo, N.; Fino, D.; Pirone, R. Study on the CO Oxidation over Ceria-Based Nanocatalysts. *Nanoscale Res. Lett.* **2016**, *11*, 165. [[CrossRef](#)]
41. Lykaki, M.; Pachatouridou, E.; Carabineiro, S.A.; Iliopoulou, E.; Andriopoulou, C.; Kallithrakas-Kontos, N.; Boghosian, S.; Konsolakis, M. Ceria nanoparticles shape effects on the structural defects and surface chemistry: Implications in CO oxidation by Cu/CeO₂ catalysts. *Appl. Catal. B Environ.* **2018**, *230*, 18–28. [[CrossRef](#)]
42. Gulyaev, R.V.; Kardash, T.Y.; Malykhin, S.E.; Stonkus, O.A.; Ivanova, A.S.; Boronin, A.I. The local structure of Pd_xCe_{1-x}O_{2-x-δ} solid solutions. *Phys. Chem. Chem. Phys.* **2014**, *16*, 13523–13539. [[CrossRef](#)] [[PubMed](#)]
43. Popović, Z.; Dohčević-Mitrović, Z.; Šćepanović, M.; Grujić-Brojčin, M.; Aškrabić, S. Raman scattering on nanomaterials and nanostructures. *Ann. Phys.* **2011**, *523*, 62–74. [[CrossRef](#)]
44. Yao, Y.F.Y. Ceria in automotive exhaust catalysts I. Oxygen storage. *J. Catal.* **1984**, *86*, 254–265. [[CrossRef](#)]
45. Giordano, F.; Trovarelli, A.; de Leitenburg, C.; Giona, M. A Model for the Temperature-Programmed Reduction of Low and High Surface Area Ceria. *J. Catal.* **2000**, *193*, 273–282. [[CrossRef](#)]

46. Kurnatowska, M.; Kepinski, L.; Mista, W. Structure evolution of nanocrystalline $Ce_{1-x}Pd_xO_{2-y}$ mixed oxide in oxidizing and reducing atmosphere: Reduction-induced activity in low-temperature CO oxidation. *Appl. Catal. B Environ.* **2012**, *117–118*, 135–147. [[CrossRef](#)]
47. Romeo, M.; Bak, K.; El Fallah, J.; Le Normand, F.; Hilaire, L. XPS Study of the reduction of cerium dioxide. *Surf. Interface Anal.* **1993**, *20*, 508–512. [[CrossRef](#)]
48. Jain, R.; Dubey, A.; Ghosal, M.K.; Gopinath, C.S. Gas–solid interaction of $H_2-Ce_{0.95}Zr_{0.05}O_2$: New insights into surface participation in heterogeneous catalysis. *Catal. Sci. Technol.* **2015**, *6*, 1746–1756. [[CrossRef](#)]
49. Militello, M.C.; Simko, S.J. Elemental Palladium by XPS. *Surf. Sci. Spectra* **1994**, *3*, 387–394. [[CrossRef](#)]
50. Militello, M.C.; Simko, S.J. Palladium Oxide (PdO) by XPS. *Surf. Sci. Spectra* **1997**, *3*, 395–401. [[CrossRef](#)]
51. Blomberg, S.; Hoffmann, M.J.; Gustafson, J.; Martin, N.M.; Fernandes, V.R.; Borg, A.; Liu, Z.; Chang, R.; Matera, S.; Reuter, K.; et al. In Situ X-Ray Photoelectron Spectroscopy of Model Catalysts: At the Edge of the Gap. *Phys. Rev. Lett.* **2013**, *110*, 117601. [[CrossRef](#)] [[PubMed](#)]
52. Haerle, R.; Riedo, E.; Pasquarello, A.; Baldereschi, A. sp^2/sp^3 hybridization ratio in amorphous carbon from C1s core-level shifts: X-ray photoelectron spectroscopy and first-principles calculation. *Phys. Rev. B* **2001**, *65*, 045101. [[CrossRef](#)]
53. Oh, S.-H.; Hoflund, G.B. Chemical State Study of Palladium Powder and Ceria-Supported Palladium during Low-Temperature CO Oxidation. *J. Phys. Chem. A* **2006**, *110*, 7609–7613. [[CrossRef](#)] [[PubMed](#)]
54. Pillo, T.; Zimmermann, R.; Steiner, P.; Hüfner, S. The electronic structure of PdO found by photoemission (UPS and XPS) and inverse photoemission (BIS). *J. Phys. Condens. Matter* **1997**, *9*, 3987–3999. [[CrossRef](#)]
55. Slavinskaya, E.; Gulyaev, R.; Zadesenets, A.; Stonkus, O.; Zaikovskii, V.; Shubin, Y.V.; Korenev, S.; Boronin, A. Low-temperature CO oxidation by Pd/CeO₂ catalysts synthesized using the coprecipitation method. *Appl. Catal. B Environ.* **2014**, *166–167*, 91–103. [[CrossRef](#)]
56. Muravev, V.; Spezzati, G.; Su, Y.-Q.; Parastaev, A.; Chiang, F.-K.; Longo, A.; Escudero, C.; Kosinov, N.; Hensen, E.J.M. Interface dynamics of Pd–CeO₂ single-atom catalysts during CO oxidation. *Nat. Catal.* **2021**, *4*, 469–478. [[CrossRef](#)]
57. Schiller, F.; Ilyn, M.; Pérez-Dieste, V.; Escudero, C.; Huck-Iriart, C.; del Arbol, N.R.; Hagman, B.; Merte, L.R.; Bertram, F.; Shipilin, M.; et al. Catalytic Oxidation of Carbon Monoxide on a Curved Pd Crystal: Spatial Variation of Active and Poisoning Phases in Stationary Conditions. *J. Am. Chem. Soc.* **2018**, *140*, 16245–16252. [[CrossRef](#)]
58. Teschner, D.; Borsodi, J.; Wootsch, A.; Révay, Z.; Havecker, M.; Knop-Gericke, A.; Jackson, S.D.; Schlogl, R. The Roles of Subsurface Carbon and Hydrogen in Palladium-Catalyzed Alkyne Hydrogenation. *Science* **2008**, *320*, 86–89. [[CrossRef](#)]
59. Newton, M.A.; Di Michiel, M.; Kubacka, A.; Fernández-García, M. Combining Time-Resolved Hard X-ray Diffraction and Diffuse Reflectance Infrared Spectroscopy To Illuminate CO Dissociation and Transient Carbon Storage by Supported Pd Nanoparticles during CO/NO Cycling. *J. Am. Chem. Soc.* **2010**, *132*, 4540–4541. [[CrossRef](#)]
60. Westerström, R.; Messing, M.E.; Blomberg, S.; Hellman, A.; Grönbeck, H.; Gustafson, J.; Martin, N.M.; Balmes, O.; van Rijn, R.; Andersen, J.N.; et al. Oxidation and reduction of Pd(100) and aerosol-deposited Pd nanoparticles. *Phys. Rev. B* **2011**, *83*, 115440. [[CrossRef](#)]
61. Andersen, J.N.; Qvarford, M.; Nyholm, R.; Sorensen, S.L.; Wigren, C. Surface core-level shifts as a probe of the local overlayer structure: CO on Pd(100). *Phys. Rev. Lett.* **1991**, *67*, 20–23. [[CrossRef](#)] [[PubMed](#)]
62. Velasco-Vélez, J.J.; Teschner, D.; Girgsdies, F.; Hävecker, M.; Streibel, V.; Willinger, M.G.; Cao, J.; Lamoth, M.; Frei, E.; Wang, R.; et al. The Role of Adsorbed and Subsurface Carbon Species for the Selective Alkyne Hydrogenation over a Pd-Black Catalyst: An Operando Study of Bulk and Surface. *Top. Catal.* **2018**, *61*, 2052–2061. [[CrossRef](#)] [[PubMed](#)]
63. Chen, X.; Wang, X.; Fang, D. A review on C1s XPS-spectra for some kinds of carbon materials. *Full-Nanotub. Carbon Nanostruct.* **2020**, *28*, 1048–1058. [[CrossRef](#)]
64. Pozdnyakova, O.; Teschner, D.; Wootsch, A.; Kröhnert, J.; Steinhauer, B.; Sauer, H.; Toth, L.; Jentoft, F.; Knop-Gericke, A.; Paál, Z. Preferential CO oxidation in hydrogen (PROX) on ceria-supported catalysts, part II: Oxidation states and surface species on Pd/CeO₂ under reaction conditions, suggested reaction mechanism. *J. Catal.* **2006**, *237*, 17–28. [[CrossRef](#)]
65. Otto, K.; Haack, L.; Devries, J. Identification of two types of oxidized palladium on γ -alumina by X-ray photoelectron spectroscopy. *Appl. Catal. B Environ.* **1992**, *1*, 1–12. [[CrossRef](#)]
66. Kibis, L.S.; Stadnichenko, A.I.; Koscheev, S.V.; Zaikovskii, V.I.; Boronin, A.I. Highly Oxidized Palladium Nanoparticles Comprising Pd⁴⁺ Species: Spectroscopic and Structural Aspects, Thermal Stability, and Reactivity. *J. Phys. Chem. C* **2012**, *116*, 19342–19348. [[CrossRef](#)]
67. Bera, P.; Patil, K.; Jayaram, V.; Subbanna, G.; Hegde, M. Ionic Dispersion of Pt and Pd on CeO₂ by Combustion Method: Effect of Metal–Ceria Interaction on Catalytic Activities for NO Reduction and CO and Hydrocarbon Oxidation. *J. Catal.* **2000**, *196*, 293–301. [[CrossRef](#)]
68. Misch, L.M.; Kurzman, J.A.; Derk, A.R.; Kim, Y.-I.; Seshadri, R.; Metiu, H.; McFarland, E.W.; Stucky, G.D. C–H Bond Activation by Pd-substituted CeO₂: Substituted Ions versus Reduced Species. *Chem. Mater.* **2011**, *23*, 5432–5439. [[CrossRef](#)]
69. Zhou, G.-F.; Ma, J.; Bai, S.; Wang, L.; Guo, Y. CO catalytic oxidation over Pd/CeO₂ with different chemical states of Pd. *Rare Met.* **2020**, *39*, 800–805. [[CrossRef](#)]

70. Liu, B.; Liu, J.; Li, T.; Zhao, Z.; Gong, X.-Q.; Chen, Y.; Duan, A.; Jiang, G.; Wei, Y. Interfacial Effects of CeO₂-Supported Pd Nanorod in Catalytic CO Oxidation: A Theoretical Study. *J. Phys. Chem. C* **2015**, *119*, 12923–12934. [[CrossRef](#)]
71. Chen, Y.; Chen, J.; Qu, W.; George, C.; Aouine, M.; Vernoux, P.; Tang, X. Well-defined palladium–ceria interfacial electronic effects trigger CO oxidation. *Chem. Commun.* **2018**, *54*, 10140–10143. [[CrossRef](#)] [[PubMed](#)]

Disclaimer/Publisher’s Note: The statements, opinions and data contained in all publications are solely those of the individual author(s) and contributor(s) and not of MDPI and/or the editor(s). MDPI and/or the editor(s) disclaim responsibility for any injury to people or property resulting from any ideas, methods, instructions or products referred to in the content.